Rotational motions from the 2016, Central Italy seismic sequence, as observed by an underground ring laser gyroscope

A. Simonelli,[1,2] H. Igel,[1] J. Wassermann,[1] J. Belfi,[2] A. Di Virgilio,[2] N. Beverini,[2] G. De Luca[3] and G. Saccorotti[4]

[1]*Department of Earth and Environmental Sciences, Ludwig-Maximilians-University Munich, Theresienstrasse 4, D-80333, Munich, Germany. E-mail:*
andrea.simonelli.as@gmail.com
[2]*Istituto Nazionale di Fisica Nucleare, Sezione di Pisa, Largo Pontecorvo 3, 56127 Pisa, Italy.*
[3]*Istituto Nazionale di Geofisica e Vulcanologia, Centro Nazionale Terremoti, Via di Vigna Murata 105, 00143 Roma, Italy.*
[4]*Istituto Nazionale di Geofisica e Vulcanologia, Sezione di Pisa, Via della Faggiola 32, 56126 Pisa, Italy*

SUMMARY

We present the analysis of rotational and translational ground motions from earthquakes recorded during October–November 2016, in association with the Central Italy seismic sequence. We use co-located measurements of the vertical ground rotation rate from a large ring laser gyroscope and the three components of ground velocity from a broad-band seismometer. Both instruments are positioned in a deep underground environment, within the Gran Sasso National Laboratories of the Istituto Nazionale di Fisica Nucleare. We collected dozens of events spanning the 3.5–5.9 magnitude range and epicentral distances between 30 and 70 km. This data set constitutes an unprecedented observation of the vertical rotational motions associated with an intense seismic sequence at local distance. Under the plane-wave approximation we process the data set in order to get an experimental estimation of the events backazimuth. Peak values of rotation rate (PRR) and horizontal acceleration (PGA) are markedly correlated, according to a scaling constant which is consistent with previous measurements from different earthquake sequences. We used a prediction model in use for Italy to calculate the expected PGA at the recording site, obtaining consequently predictions for PRR. Within the modelling uncertainties, predicted rotations are consistent with the observed ones, suggesting the possibility of establishing specific attenuation models for ground rotations, like the scaling of peak velocity and peak acceleration in empirical ground-motion prediction relationships. In a second step, after identifying the direction of the incoming wavefield, we extract phase-velocity data using the spectral ratio of the translational and rotational components. This analysis is performed over time windows associated with the *P*-coda, *S*-coda and *Lg* phase. Results are consistent with independent estimates of shear wave velocities in the shallow crust of the Central Apennines.

Key words: Rotational seismology; Surface waves and free oscillations; Wave propagation.

1 INTRODUCTION

On 2016 August 24, at 01:36:32 UTC an M_w=6.0 struck the central sector of the Apennines chain, Italy (see Michele *et al.* 2016), causing almost 300 casualties and extensive destruction. During the following 2 months, both rate and energy of aftershocks decreased progressively. On 2016 October 26, the activity renewed with two energetic events (M_w=5.4 and M_w=5.9) until climaxing, 4 d later, with an M_w=6.5 shock (see Chiaraluce *et al.* 2017). A significant portion of this latter activity was recorded by the Gingerino large ring laser gyroscope (RLG), installed within the Laboratori Nazionali del Gran Sasso (LNGS), the underground laboratory of the Italian National Institute for Nuclear Physics (INFN). The RLG operates jointly with a broad-band seismometer, thus allowing the contemporaneous recording of ground rotation and translations during the transit of seismic waves. The co-located observation of ground three-component translations and vertical rotations permits, with a single station approach, to estimate the backazimuth (hereinafter BAZ) of the incoming wavefield generated by seismic events as well as the phase velocity for the *Lg* regional phase and horizontally polarized shear waves. The latter ones can be generated by the *P*–*SH* conversion after the onset of the *P* phase (*P*-coda) and are present in the *S*-coda itself. The seismological observations of rotational motions by means of large RLGs (see Schreiber & Wells 2013) started
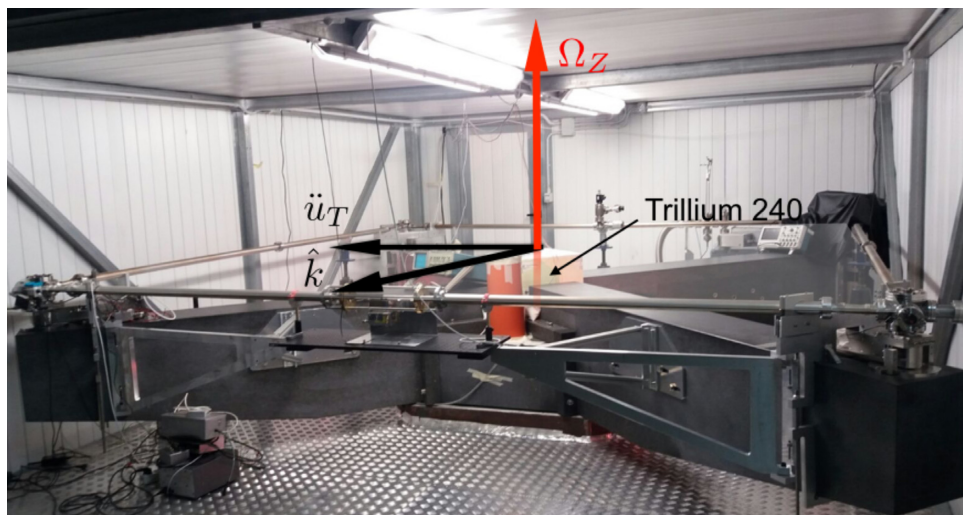
Figure 1. The Gingerino RLG and the seismometer Trillium 240 in the central light yellow box. The arrows indicate the observables that are object of this study, that is, vertical rotation rate in red (from the RLG), transverse acceleration in black (after processing the seismometer data) and the direction of the wavefield $\hat{k}$. In this example, the vectors $\hat{k}$ and $\ddot{u}_T$ point to the north and to the east, respectively. They correspond to a shear wave propagating to the north direction causing a transverse acceleration along the E–W direction.
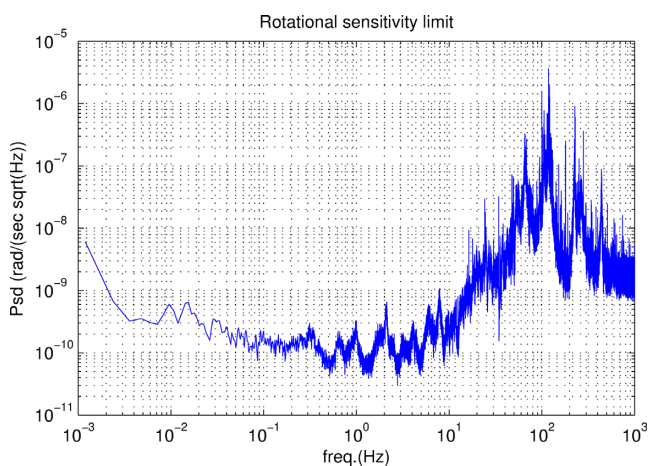

Figure 2. The rotational sensitivity limit of the Gingerino RLG.

from the first pioneering experiments by Stedman *et al.* (1995a), McLeod *et al.* (1998) and Pancha *et al.* (2000) in New Zealand. More quantitative and extensive analyses were performed on the G-Wettzel RLG data in Igel *et al.* (2005, 2007) and Cochard *et al.* (2006). Simonelli *et al.* (2016) and Belfi *et al.* (2017) report detections and analysis of teleseismic events recorded by the Gingerino RLG. The vast majority of these previous works are based on teleseismic observations, where, under the plane-wave assumption, it was successfully shown the possibility of measuring both the event BAZ and the local phase velocity. The location of the Gingerino RLG and its sensitivity permit to measure earthquake-generated rotations from events at teleseismic distances to very local, high-amplitude shocks. As an example, the Campotosto fault system, that generated during this sequence an M_w 5.5 earthquake, is located only 20 km away from the LNGS. Under these conditions, the joint analysis of ground rotation and translations is made challenging by the higher dominant frequencies of the incoming wavefield, that is, from 2 to 5 Hz in the *S*-coda, which is an unexplored frequency range for a large RLG. The aim of this paper is to investigate,
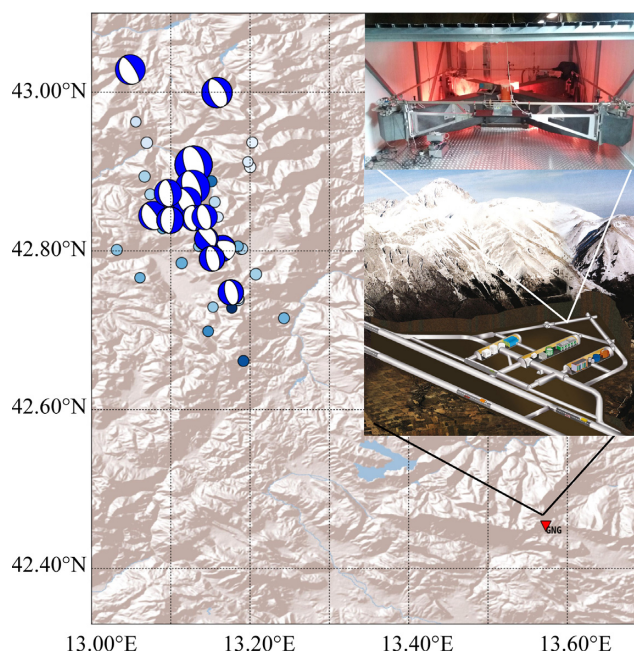

Figure 3. Map showing the epicentral locations of our data set. Beach balls indicate the focal solutions for the 10 strongest events; the size of the balls is proportional to magnitude. The red triangle marks the location of the experimental setup. The top and bottom panels in the inset respectively show the Gingerino RLG and a sketch map of the LNGS underground laboratories.

through the analysis of a unique data set, the performance of co-located rotational and translational sensors towards the wavefield characterization and source location of energetic earthquakes at local distance. On a long-term perspective, an extensive analysis of many earthquakes having a large span of epicentral distances and BAZ angles will allow us to characterize the local structure of the Gran Sasso region.

Table 1. List of earthquakes analysed in this study.

Event	Start time	Lat	Long	Mag	Dist (km)	BAZ (deg)	Depth (km)	Peak rot. rate (rad s^{-1})	Peak acc. (m s^{-2})
1	26-Oct-2016 19:18:05	42.909	13.129	5.9	62.3	324.6	7.5	1.74e-05	4.30e-02
2	26-Oct-2016 17:10:35	42.88	13.127	5.4	59.8	322.6	8.7	1.68e-05	2.72e-02
3	01-Nov-2016 07:56:36	42.999	13.158	4.8	69.5	331.0	9.9	7.26e-06	2.51e-02
4	03-Nov-2016 00:35:00	43.029	13.049	4.7	77.0	326.4	8.4	5.65e-06	1.07e-02
5	30-Oct-2016 13:34:54	42.803	13.165	4.5	51.2	319.5	9.2	2.24e-06	3.64e-03
6	30-Oct-2016 12:06:59	42.844	13.078	4.5	59.4	317.2	9.7	5.55e-06	7.88e-03
7	26-Oct-2016 21:41:59	42.861	13.128	4.5	58.1	321.4	9.9	3.88e-06	8.06e-03
8	27-Oct-2016 08:21:45	42.873	13.1	4.3	60.6	320.5	9.4	1.70e-06	3.79e-03
9	31-Oct-2016 07:05:44	42.841	13.129	4.2	56.4	320.1	10.0	2.08e-06	5.02e-03
10	30-Oct-2016 10:19:25	42.815	13.145	4.1	53.3	319.1	10.8	2.45e-06	2.24e-03
11	27-Oct-2016 03:19:26	42.844	13.15	4.0	55.5	321.6	9.2	4.56e-06	8.03e-03
12	16-Oct-2016 09:32:34	42.748	13.176	4.0	46.1	315.4	9.2	3.57e-06	6.03e-03
13	31-Oct-2016 06:17:19	42.771	13.207	3.9	46.3	319.9	9.9	1.07e-06	1.35e-03
14	27-Oct-2016 17:22:22	42.846	13.108	3.9	57.9	319.1	9.0	9.18e-07	4.19e-03
15	08-Oct-2016 18:11:08	42.738	13.185	3.9	44.8	315.1	9.5	1.73e-06	2.97e-03
16	07-Nov-2016 18:56:15	42.888	13.151	3.8	59.4	324.6	8.1	3.23e-06	4.40e-03
17	28-Oct-2016 15:56:58	42.788	13.119	3.8	52.6	315.2	9.8	1.84e-06	3.43e-03
18	26-Oct-2016 19:43:42	42.893	13.069	3.8	63.9	320.1	12.6	1.61e-06	2.44e-03
19	09-Nov-2016 06:13:09	42.661	13.192	3.7	38.8	306.7	10.7	4.18e-06	4.93e-03
20	30-Oct-2016 12:32:56	42.715	13.243	3.7	39.7	317.3	8.2	8.28e-07	7.40e-04
21	30-Oct-2016 11:14:20	42.803	13.19	3.7	49.9	321.3	9.4	1.42e-06	1.90e-03
22	28-Oct-2016 19:56:31	42.866	13.162	3.7	56.9	323.9	13.2	1.51e-06	2.61e-03
23	26-Oct-2016 21:24:51	42.867	13.078	3.7	61.3	318.8	10.3	2.41e-06	3.32e-03
24	06-Nov-2016 18:15:17	42.806	13.185	3.6	50.5	321.2	8.9	7.63e-07	1.32e-03
25	05-Nov-2016 08:17:39	42.699	13.147	3.6	44.3	308.2	11.1	1.29e-06	7.50e-04
26	31-Oct-2016 09:34:16	42.816	13.151	3.6	53.1	319.6	9.2	1.25e-06	1.33e-03
27	30-Oct-2016 23:56:19	42.828	13.09	3.6	57.4	316.7	7.9	1.40e-06	2.20e-03
28	30-Oct-2016 10:26:24	42.836	13.071	3.6	59.1	316.2	10.8	1.21e-06	1.40e-03
29	09-Oct-2016 04:42:42	42.74	13.185	3.6	45.0	315.3	11.8	7.65e-07	1.17e-03
30	02-Nov-2016 06:41:12	42.796	13.167	3.5	50.6	319.1	10.3	6.14e-07	5.42e-04
31	01-Nov-2016 17:59:12	42.806	13.135	3.5	53.1	317.8	10.8	1.75e-06	3.08e-03
32	30-Oct-2016 13:14:16	42.766	13.061	3.5	54.4	309.9	8.7	1.00e-06	1.26e-03
33	28-Oct-2016 23:18:08	42.88	13.094	3.5	61.5	320.6	14.0	1.53e-06	2.01e-03

2 GEOLOGICAL AND STRUCTURAL FRAMEWORK

Moment tensor solutions (http://cnt.rm.ingv.it/tdmt) for the vast majority of significant quakes indicate the activation of extensional faults striking NNW–SSE and dipping 40°–50° to west. Ongoing extension in the area is testified by the analysis of crustal strain and seismicity data (Bird & Carafa 2016), yet the tectonic setting and the landscape of the region are still dominated by the contractional structures of the Neogene–Quaternary Apennines fold-and-thrust belt. The extension in the Apennines is indeed a relatively young process (e.g. Malinverno & Ryan 1986) that proceeds at the relatively slow rate of 2–3 mm yr^{-1} (Bird & Carafa 2016). Consequently, the currently active structures have not yet fully reshaped the Apennines highs-and-lows of contractional origin with extensional basin- and range-type landforms. It is worth recalling that some of the well-exposed extensional faults, generally bounding an intermountain basin, were created by a pre-orogenic (Mesozoic) or by a synorogenic extensional (Miocene) regime and were shifted to their present location during the Neogene thrusting phase, for instance, through a shortcut mechanism (positive inversion tectonics; e.g. Tavarnelli 1996; Butler et al. 2006; Scisciani & Calamita 2009). The complex framework described above explains why identifying and characterizing seismogenic sources in the Apennines are extremely challenging (see Di Domenica et al. 2014, for a discussion on this topic).

3 THE EXPERIMENTAL SETUP

The four-component (4-C) seismic station is constituted by the Gingerino RLG and a broad-band seismometer Trillium 240 from Nanometrics (see Fig. 1). The first instrument senses the rotations of the ground around the local vertical axis, while the latter detects ground velocity along three orthogonal axes. Gingerino is an He–Ne RLG operating at a wavelength of 632 nm. The optical cavity is a square of 3.6 m side length and is defined by four spherical mirrors with 4 m radius of curvature. The design of the corners is based on the GeoSensor project (see Schreiber et al. 2006). The alignment can be tuned by means of a micrometric system acting on the mirror chambers' orientation. More details on the instrument are described in Belfi et al. (2017). Within the active optical cavity, two laser beams are circulating in clockwise and anticlockwise directions. The perimeter represented by the path of the two beams encloses an area A. When an active cavity is rotating around an axis having an orthogonal component with respect to the area A, the optical frequencies of the two laser beams propagating in opposite directions are shifted (with respect to the non-rotating cavity) by a quantity that is proportional to the rotation rate. This is known as the Sagnac effect. The detection of this frequency shift is made easier by letting the two beams to interfere out of the optical cavity with an optical system called beam combiner. The raw data from an RLG that is fixed to the Earth ground consist in a sinusoidal interference signal whose mean frequency *f* is proportional to the Earth rotation
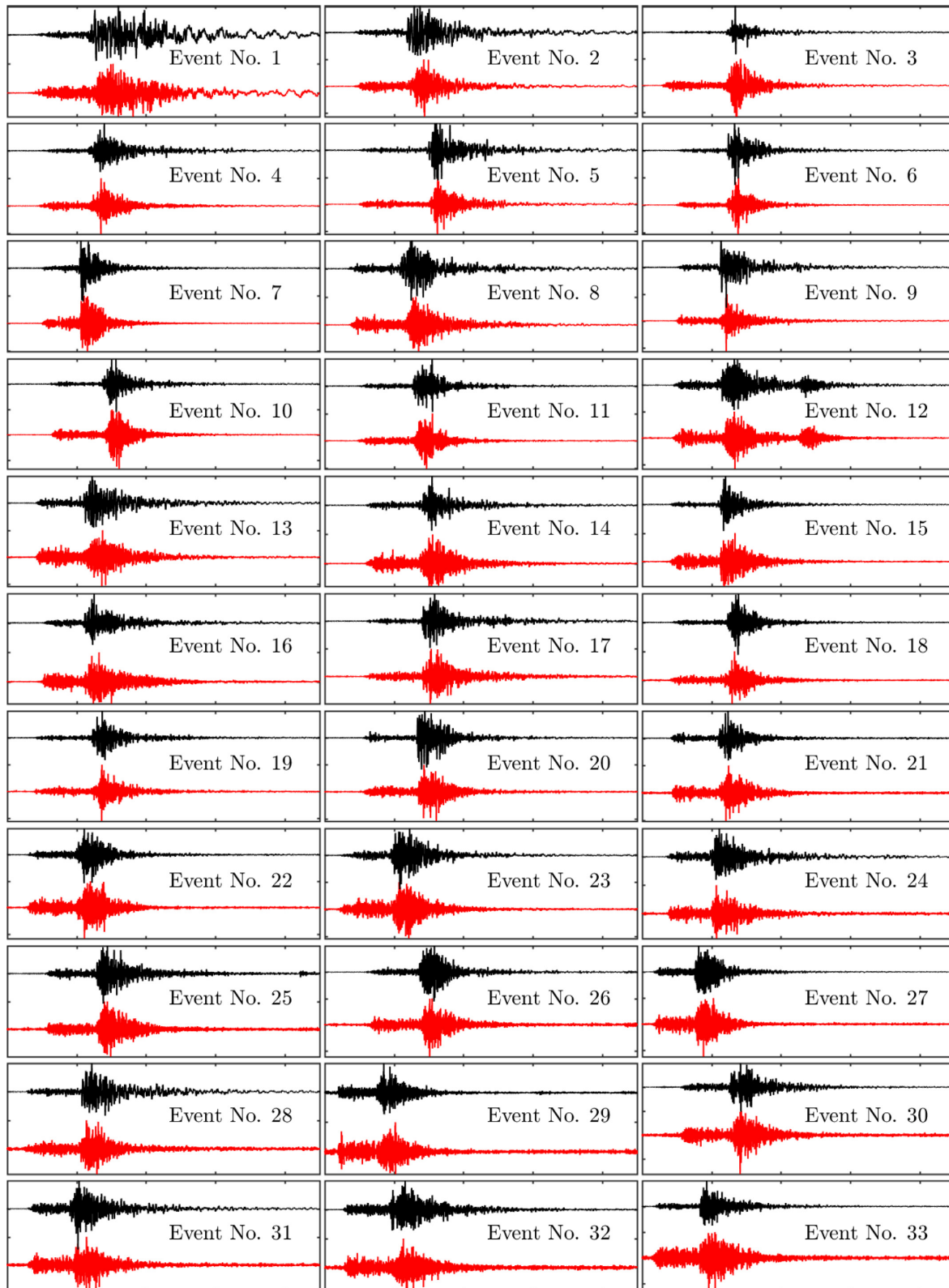
Figure 4. Waveforms of the recorded events. Red and black lines are for the vertical rotation rate and transverse acceleration, respectively. The time window is 45-s long. Individual rotational and translational traces are normalized to their respective peak value.

rate, $\Omega_\oplus$, according to eq. (1):

$$f = \frac{\Omega_\oplus A \sin\theta}{P\lambda_{\text{He:Ne}}}. \tag{1}$$

Here, $\lambda_{\text{He:Ne}}$ is the wavelength of the He:Ne laser (632 nm), P is the perimeter of the square cavity, A is the enclosed area, θ is the latitude at the experiment site and $\Omega_\oplus$ is the Earth rotation vector.
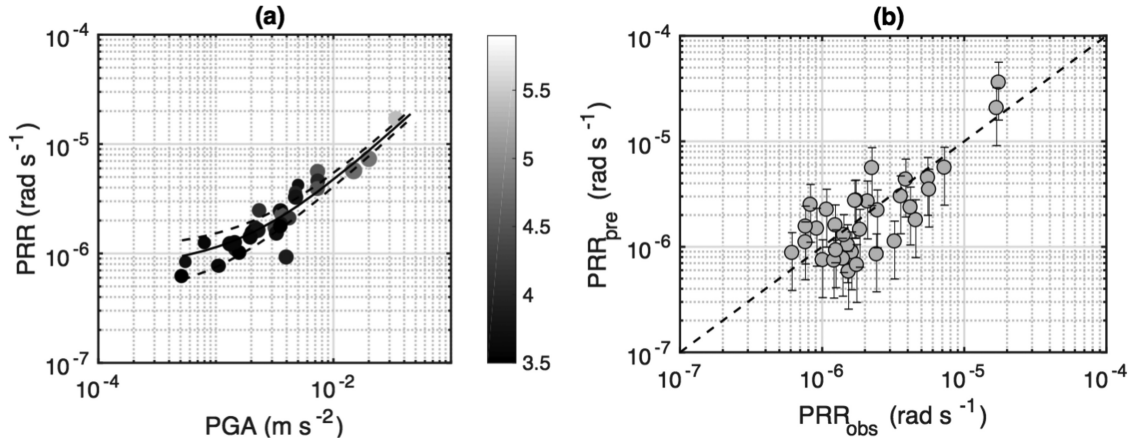
Figure 5. (a) Vertical peak ground rotation rate (PRR) versus horizontal peak ground accelerations (PGA) for the 33 earthquakes analysed in this study. Magnitudes are in grey scale according to the scale at the right; the size of the symbols is proportional to the epicentral distance. The black line is the least-squares fit to the data, with the corresponding 99 per cent confidence bounds (dashed lines). (b) Comparison of the observed ground rotation rates (PRR$_{obs}$) with those expected from Bindi *et al.* (2011) predictive relationship (PRR$_{pre}$), after application of the appropriate scaling factor between the observed PRR and PGA. Error bars include uncertainties in the predictive relationship and in the estimate of the scaling coefficient.
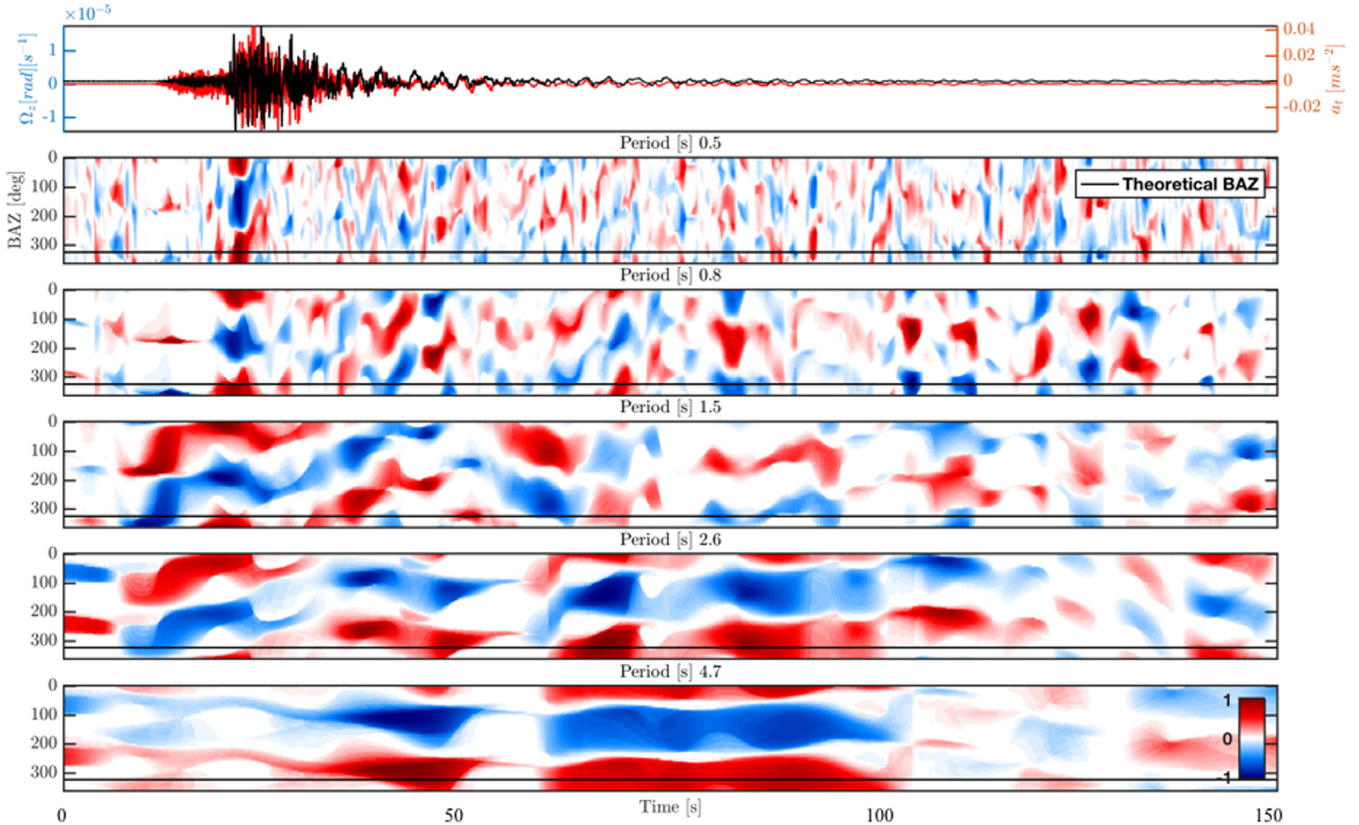

Figure 6. Backazimuth analysis in different frequency bands for the M_w=5.9 Visso earthquake. The colour scale ranges from anticorrelation (blue) to correlation (red) according to the colour bar reported in the lowermost panel. The top panel shows the superposition of the time-series of the rotation rate (red) and the transverse acceleration (black).

At the latitude of LNGS the Sagnac frequency is 280.4 Hz. During the transit of a transversally polarized seismic wave, the ground under the RLG is locally rotating and at the same time, the whole planet Earth is rotating. The Earth rotation rate is approximately 7.29 μrad s^{-1}. If the local rotation induced by a seismic event is equal to or larger than the Earth rotation rate, then dynamically the RLG encounters a phase of zero rotation. This is because the seismic rotation cancels out with the Earth's rotation. This is a very

important question about the dynamic range of the instrument. In fact we know from Stedman *et al.* (1995b) that a real RLG is affected by the lock in phenomenon, which makes it blind to rotations when the rotation rate is below a certain threshold. This threshold varies with the instrument type, for example, it depends on the size and on the quality of the cavity mirrors. In the case of our strongest recorded event, that is, the M_w 5.9 occurred on 2016 October 26, at 19:18 UTC near Visso, the maximum rotation rate induced by the

earthquake was only four times smaller than the Earth rotation rate. To conclude, the maximum peak amplitude detectable by an RLG without distortions and clipping of the waveform is in the best case equal to the Earth rotation rate.

The broad-band seismometer, installed at the centre of the RLG, is part of the national monitoring programme of the Italian Istituto Nazionale di Geofisica e Vulcanologia (INGV hereinafter), under the station code GIGS. This instrument has a flat response to velocity from 240 s to 35 Hz and has a self-noise level below the New Low Noise model (NLNM; Peterson *et al.* 1993) from 100 s to 10 Hz.

For Gingerino, we deduced an instrumental sensitivity limit at the level 100 (prad s^{-1})$\sqrt{\text{Hz}}$ in the range $[10^{-2}, -1]$ Hz (Belfi *et al.* 2017). However, the long-term stability of the raw data is limited to 10–20 s, mainly by radiation backscattering on the mirrors (Fig. 2). For additional information on the performance and characterization of the experimental setup, the reader is referred to Belfi *et al.* (2017).

4 DATA ANALYSIS

Theory (Aki & Richards 2009) predicts that the rotation angle $\vec{\Theta}$ can be obtained from the ground velocity as the curl of the wavefield $\vec{u}$:

$$\vec{\Theta} = \frac{1}{2}(\nabla \times \vec{u}). \tag{2}$$

For example, the ground velocity caused by a Love wave travelling as a plane wave along the $\hat{x}$-direction and having an angular frequency ω can be expressed through eq. (3):

$$u_y = A e^{i\omega(\frac{x}{c_L} - t)}. \tag{3}$$

Combining eq. (3) with eq. (2) yields

$$\Theta_z = \frac{-u_y}{2c_L}, \tag{4}$$

which provides a direct estimation of the phase velocity c_L from a single-site measurement as an amplitude ratio. If we differentiate eq. (4) with respect to time we can obtain the same estimation from the rotation rate/acceleration pair of observables. Since the natural output of the processing of the raw data from an RLG is a rotation rate, in literature it is more common to find this second kind of measurements. Our data set, consisting in 33 events (see Table 1), permits us to extend the vertical rotation rate/transverse acceleration analysis to regional events whose epicentral distance and magnitude range from 30 to 70 km and M_L 3.5 to M_w 5.9, respectively. In Fig. 3 we report the map of the analysed events and their epicentral location, as well as the location of the Gingerino station within the LNGS. For the most energetic 10 events we also represent the moment tensor solutions derived from INGV's Time Domain Moment Tensor catalogue (http://cnt.rm.ingv.it/tdmt) by G23. Vertical rotation rate and transverse acceleration for all the 33 earthquakes are illustrated in Fig. 4.

In the next sections, we first provide a statistical estimation of the misfit between the theoretical BAZ (i.e. the one derived from station and epicentre coordinates) and the estimated one. Then we calculate a frequency-dependent phase velocity for different seismic phases in those frequency bands where we have high correlation between vertical rotation rate and transverse acceleration. Our analyses address three separate arguments which aim at verifying the ability of the 4-D deployment to consistently retrieve the direction of the source and the phase velocity of the incoming wavefield.
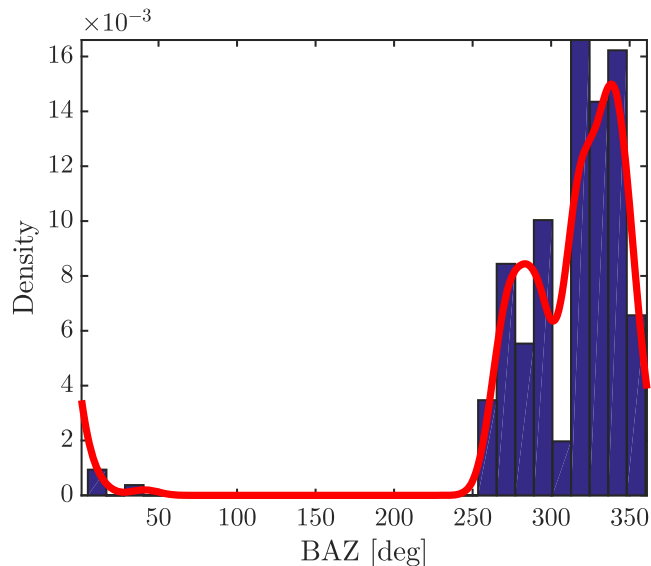

Figure 7. The M_w= 5.9, Visso earthquake: distribution of maximum correlation values in the *Lg*-wave time windows over the 2–5 s period range. The solid red line represents the KDE estimation of the distribution. For this event the theoretical BAZ is 324°.
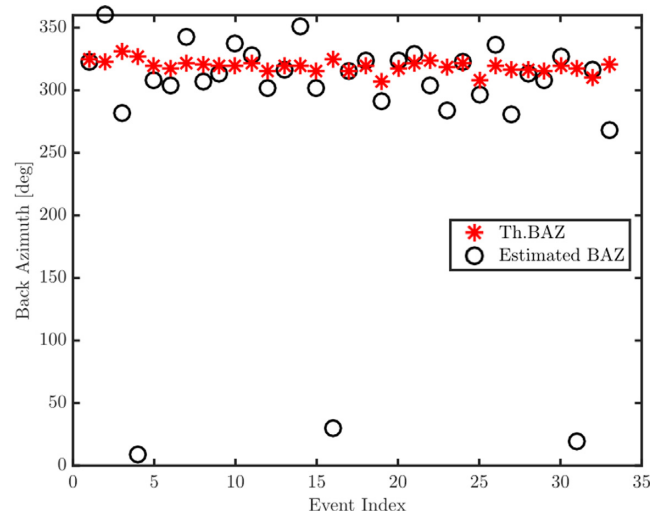

Figure 8. Theoretical and observed BAZ for all the events listed in Table 1.

4.1 Peak ground rotation and acceleration

The first step of our analyses consisted in investigating the general relationships between ground rotation and translation. We therefore compared peak values of the rotation rate (PRR) with an intensity measure commonly used in earthquake engineering, namely, the peak ground acceleration (PGA). Using the time derivative of the ground-velocity seismograms recorded by the seismometer, we estimated PGA as the geometric mean of the peak values measured separately at the two horizontal components of motion (e.g. Douglas 2003). As expected, PGA and PRR are highly correlated (Fig. 5a); using least-squares, we fit the data with a straight line in the form PRR = $a \cdot$ PGA + b, where the slope a has the unit dimension of slowness (s m^{-1}). Its scaled inverse $c = 1/(2a)$ has been termed apparent velocity after Spudich & Fletcher (2008); it is not necessarily a true phase velocity, but rather a scaling factor characterizing the seismic wavefield beneath the recording station. Results of the fitting yield $a = 4 \times 10^{-4} \pm 1.5 \times 10^{-5}$ s m^{-1} and
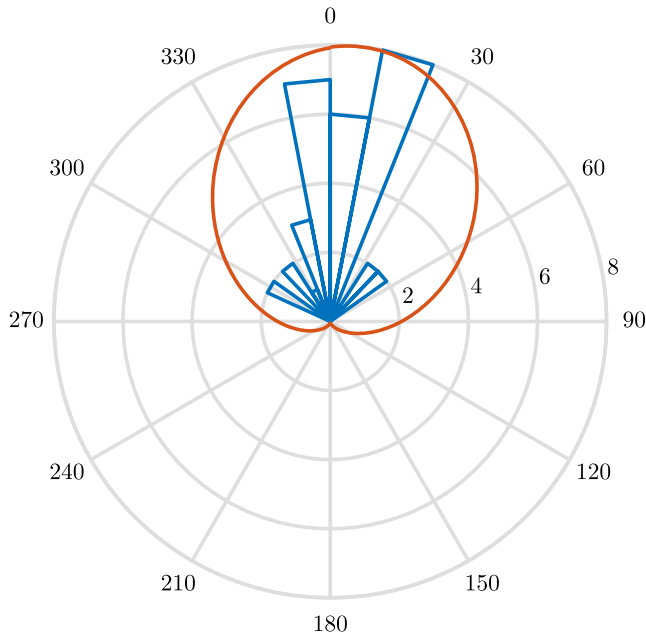
Figure 9. Misfit distribution and the relative Gaussian KDE modelling in the solid red line.

$b = 7 \times 10^{-7} \pm 2 \times 10^{-7}$ s^{-1}. Our estimate of the scaling coefficient is comparable to the value of 4.72×10^{-4} s m^{-1} found from an earthquake data set recorded at the HWLB station, Taiwan (see Lee *et al.* 2012). The corresponding apparent velocity c is equal to 1250 m s^{-1}, which compares well with the 700–1700 m s^{-1} range found by Spudich & Fletcher (2008) for the 2004 Parkfield events recorded at the UPSAR seismic array.

The tight correlation between PGA and PRR shown in Fig. 5(a) suggests that PRRs might scale with magnitude, distance, site geology and fault type like the scaling of peak velocity and peak acceleration in empirical ground-motion prediction relationships. For each earthquake, we then used the prediction model in use for Italy by Bindi *et al.* (2011) to calculate the expected PGA at the recording site under the assumption of soil class A (hard rock) and normal style-of-faulting. Using the above scaling coefficient a, we then derived predictions for PRR. The results are shown in Fig. 5(b); most predicted rotations are consistent with the observed data, once accounting for the uncertainties in the predictive relationship and in the estimate of the scaling coefficients.

Due to the intrinsic difficulties in their measurement, ground rotations are not currently included in any assessment of shaking intensities. However, once a more comprehensive set of rotational observations will be available, the above results indicate the possibility of establishing specific attenuation models for ground rotations, like the scaling of peak velocity and peak acceleration in empirical ground-motion prediction relationships. This would allow including ground rotations into hazard maps and, consequently, building codes.

4.2 Backazimuth estimation

The horizontal components of ground acceleration are rotated in steps $\delta\theta$ of 1° within the range $[0,2\pi]$ and the radial and transverse acceleration components are calculated i.e. : $\{\ddot{u}_R(\theta), \ddot{u}_T(\theta)\}$, where θ is the trial BAZ. Assuming that the hypothesis of plane-wave propagation and linear elasticity holds, vertical rotation and

transverse acceleration (Cochard *et al.* 2006; Aki & Richards 2009) should manifest themselves with the same waveform scaled by the frequency-dependent phase velocity $C(f)$ (see eq. 4). We use the Wavelet coherence tool (WTC; Grinsted *et al.* 2004) to obtain time-frequency maps of correlation between the vertical rotation rate Ω_z and the transverse acceleration set $\{\ddot{u}_T(\theta)\}$, obtained by the rotations described above. The result of this processing is an array of correlation values $C(\theta, t, f)$ that are functions of time and frequency and the trial BAZ of the seismometer horizontal components. This representation allows us to obtain a time-frequency estimation of the BAZ. This analysis is shown in Fig. 6 in the case of the Visso M_w 5.9 earthquake. The solid line in Fig. 6 represents the theoretical BAZ. For this event the *Lg* waves are very clear in both rotational and translational traces and, at periods longer than 3 s, the estimated BAZ is in good agreement with the theoretical one. In the frequency band around 2 Hz, a region of high coherence identifies the *SH*-wave arrival, whose BAZ corresponds to the theoretical one. A more quantitative and statistically consistent analysis of the BAZ for the entire event database is described hereinafter. The WTC(θ, t, f) array is calculated for every event. We find the maxima of correlation in a time window that goes from the beginning of the *S*-coda to the end of the surface wave phase. The obtained values are binned in histograms and the distribution is modelled with a Gaussian function (KDE Gaussian). In Fig. 7, we show the histogram and the Gaussian KDE for the Visso earthquake. For this event, surface waves are well-defined, and the best agreement between predicted and observed BAZ is observed in concomitance of the *Lg*-wave time-frequency window. We apply this processing to all the events and we resume the analysis by plotting the estimated BAZ and the theoretical one for the entire set in Fig. 8. In Fig. 9, we represent the polar histogram of the misfits and the relative Gaussian kernel modelling of the distribution. We outline that the theoretical BAZ is just an indication of the possible direction of the wavefield. As a matter of fact, once accounting for lateral velocity variations, the complex topography and the underground setting of our instruments, the propagation direction of surface waves may differ significantly from the expected one. From the analysis of teleseismic Love waves at periods longer than 10 s, Simonelli *et al.* (2016) observed a misfit of about 5°. From the analysis on the present data set, we observe a systematic, average misfit of about 10°. This can be attributed to misorientation of the seismometer, a propagation effect or a combination of both factors. We tried a cluster analysis in order to check if the misfit could be dependent on the events parameters (see Table 1) and on the signal-to-noise-ratio (SNR), but the result does not show any clear dependence. Future measurements with a triaxial fibre optic gyroscope, used as a gyroscopic compass, will allow us to orient the seismometer with a precision lower than 0.1°. By the same token, the future recording of sources at different BAZ will help clarifying possible ray-path distortions due to lateral velocity heterogeneities.

4.3 Phase-velocity estimation

Result from the above processing is to identify the BAZ angles for all the events. By applying a rotation matrix to the horizontal components of ground acceleration recorded by the seismometer (recorded in the geographical coordinates i.e. northeast) we can calculate the transverse (a_T) and longitudinal components (a_R) for every event. Only the transverse acceleration component is then used in our processing as predicted by eq. (5). For retrieving phase-velocity data from our joint rotational–translational measurements, we use the
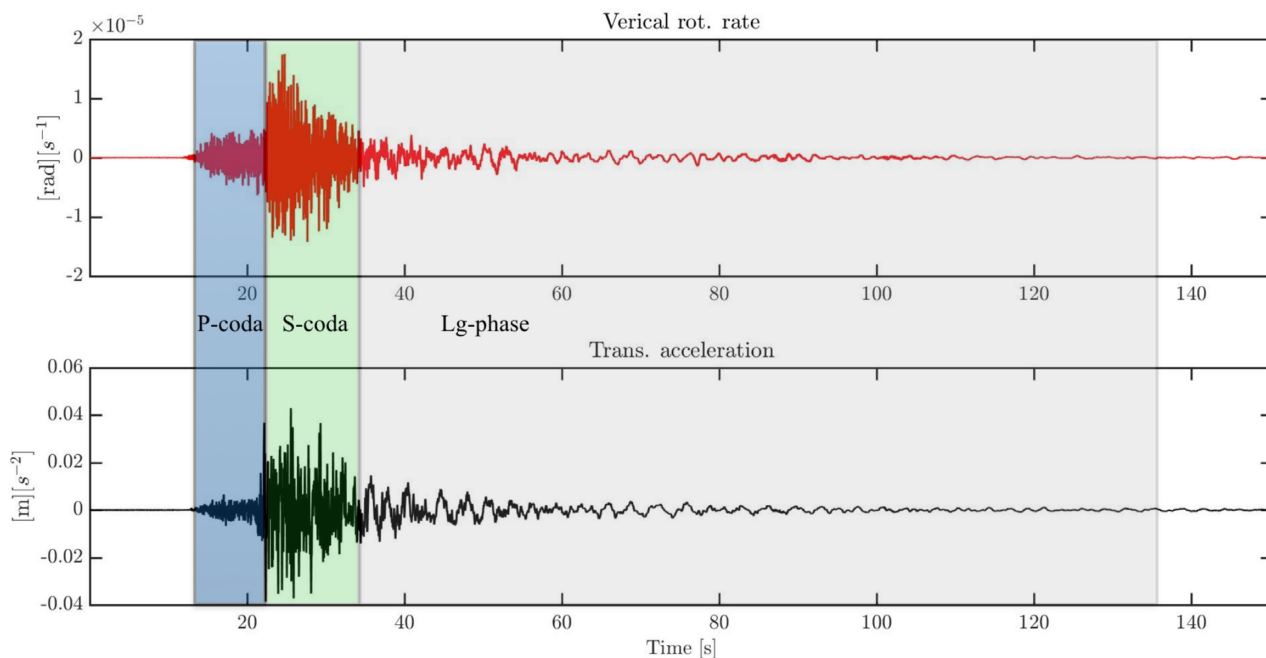
Figure 10. The rotational (red) and translational (black) components of the Visso earthquake. Coloured regions mark the time windows used for the phase-velocity study.
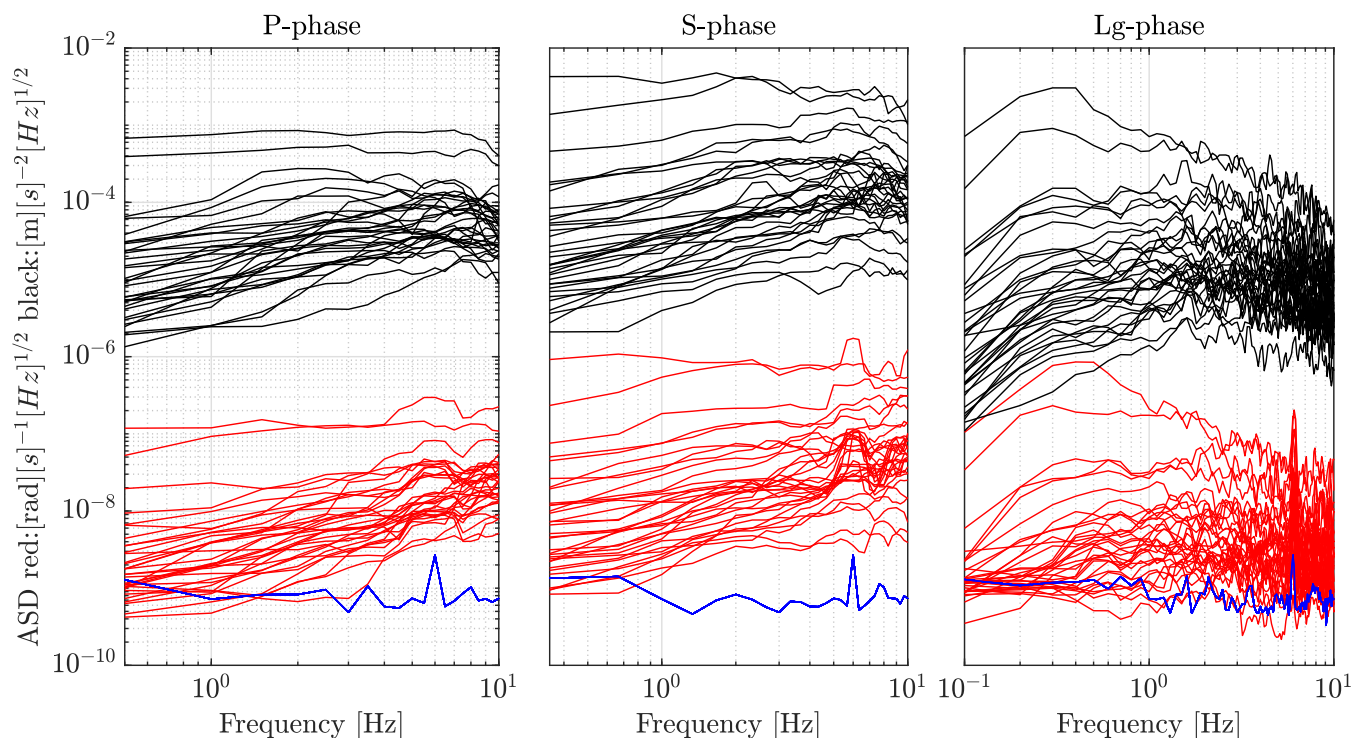

Figure 11. Amplitude spectral densities from application of the multitaper method. Black and red lines are for the transverse acceleration and vertical rotation rate, respectively. The blue line marks the noise level of the RLG. The three panels correspond to the three different time windows (seismic phases) analysed.

frequency-domain formulation of eq. (5). In order to extend the estimates to distinct seismic phases, we segment the seismograms into three consecutive time windows, which are illustrated in Fig. 10 for the sample case of the M_w 5.9 Visso earthquake. The first window spans the time interval in between the *P*- and *SH*-wave arrivals, thus including the *P*–*SH* conversion in the *P*-coda. The second window goes from the *SH* arrival, as identified in the rotational trace, to

end of the *S*-coda. The last window spans the later portion of the seismogram, which should be dominated by surface waves of the regional *Lg* phase.

For each time window of each event, we computed the amplitude spectral densities (ASDs) of the signals using the multitaper method of Thomson (1982), with a time/half-bandwidth product of eight. The whole set of ASD estimates for the rotational and translational
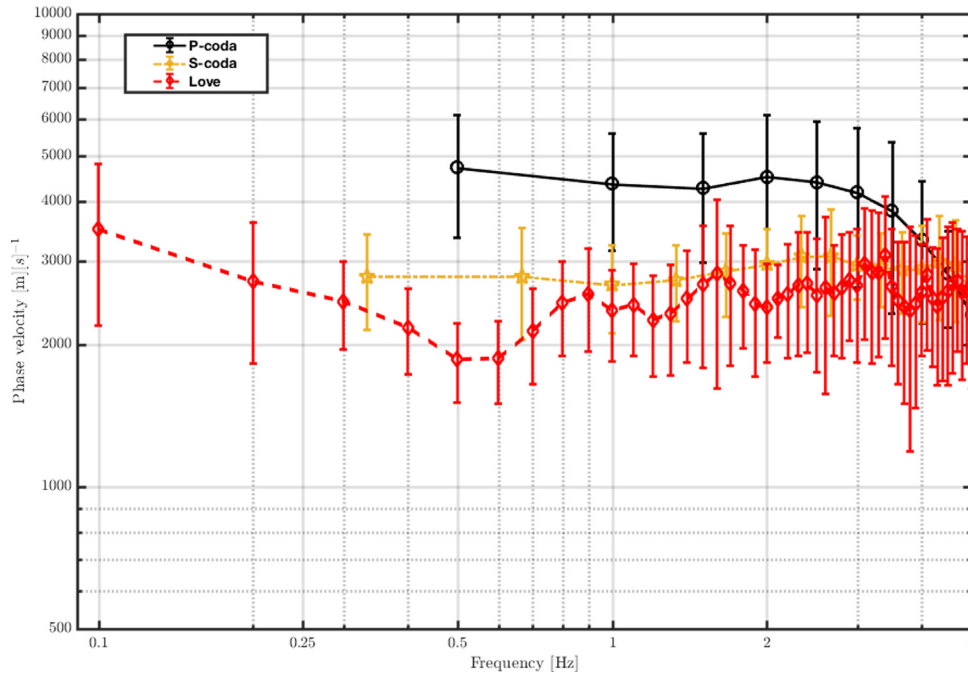
Figure 12. The result of the phase-velocity estimation method applied to *P*-coda, *S*-coda and *Lg*-wave time windows.

components is shown in Fig. 11. Phase-velocity estimates for the generic *j*th time window (seismic phase) at the *k*th frequency are then obtained as the average of the spectral ratios calculated over the *N* events:

$$C_j(f_k) = N^{-1} \sum_{i=1}^{N} c_j(f_k) = N^{-1} \sum_{i=1}^{N} \frac{a_T(f_k)}{2\Omega_z(f_k)}. \tag{5}$$

The analysis is limited to the [0.125–4 Hz] frequency band, since this is the spectral region where the translational and rotational components exhibit significant (>0.7) coherence, as evidenced by visual inspection of the WTC between Ω_z and $\ddot{u}_T$.

For the calculation of the average in eq. (5), we omitted those spectral coefficients at which the rotational ASD estimates had an SNR lower than 2. The well-known fact that the noise level of an instrument is frequency-dependent justifies the choice of applying this selection criterion. The final result of the phase-velocity analysis is shown in Fig. 12. The error for the value of $C_j(f_k)$ at the discrete frequency f_k and for the phase *j* is quantified as the standard deviation of the estimates derived for individual events. For the *Lg* time window we observe a normal dispersion curve from 0.1 to 1 Hz, which is expected given the dispersive nature of this kind of guided crustal waves. For the *P*-coda, we observe a general less dispersive behaviour associated with a larger error. For the *S*-coda, we find a pretty constant value of 2.8 km s⁻¹, with uncertainties which are generally lower than those observed for the *P*-coda. This estimate is consistent with the results of the ambient noise tomography by Li *et al.* (2010), who report shear wave velocity on the order of 2.4–2.8 km s⁻¹ for the shallowest 5 km of the crust beneath the Central Apennines. For the Visso earthquake, we also provide the phase-velocity analysis in the time domain (Fig. 13). This representation allows us to easily check the correlation between rotation and acceleration in bandpass-filtered time windows by visual inspection. For each period range, phase velocities are estimated from the ratio of the peak values of the acceleration and rotation envelopes. Phase velocities obtained by this method are in agreement with the ones obtained using the spectral ratio method described above.

5 CONCLUSIONS

This work presented the results from the operation of Gingerino, an RLG co-located with a broad-band seismometer inside the LNGS. Our data constitute some of the very first observations of earthquake-generated rotational motions associated with an energetic seismic sequence at local distance. We thus extended the application of roto-translational observations of ground motion to local events, thus exploring higher frequency ranges and larger rotation rate amplitudes. PRR and PGA are correlated according to a scaling coefficient (apparent velocity) which is consistent with previous determinations (e.g. Spudich & Fletcher 2008; Lee *et al.* 2012). Expected rotation rates derived from a ground-motion predictive relationship in use for Italy in Bindi *et al.* (2011) are compatible with the observed ones. This opens the way to the establishment of attenuation models for ground rotations, like the scaling of peak velocity and peak acceleration in empirical ground-motion prediction relationships. The Wavelet coherence is used as a filter for identifying those regions of the time-period representation where the rotation rate and transverse acceleration signals exhibit significant coherence. The BAZ of the observed events has been estimated and compared to the predicted ones. This analysis confirms that also at regional distances we are able, by using 4-C observations, to find the direction of the wavefield with an error that has been quantified through the misfit distribution. This analysis shows a systematic mean value of 10° of misfit that can be due to both, a misalignment of the seismometer or to a structural effect. In a second step, after finding the set of BAZ angles, we oriented our seismometer components according to the ray parameters. We divided the seismograms in three different time windows that identify the *P*-coda, *S*-coda and *Lg* phases. For each time window and for all the events we calculated the amplitude spectral densities, both for transverse acceleration and vertical rotation rate. The spectral ratio of transverse acceleration and twice the rotation rate allowed to retrieve estimates of phase velocities over the period range spanned by correlated arrivals. Coherency among ground rotation and translation is also
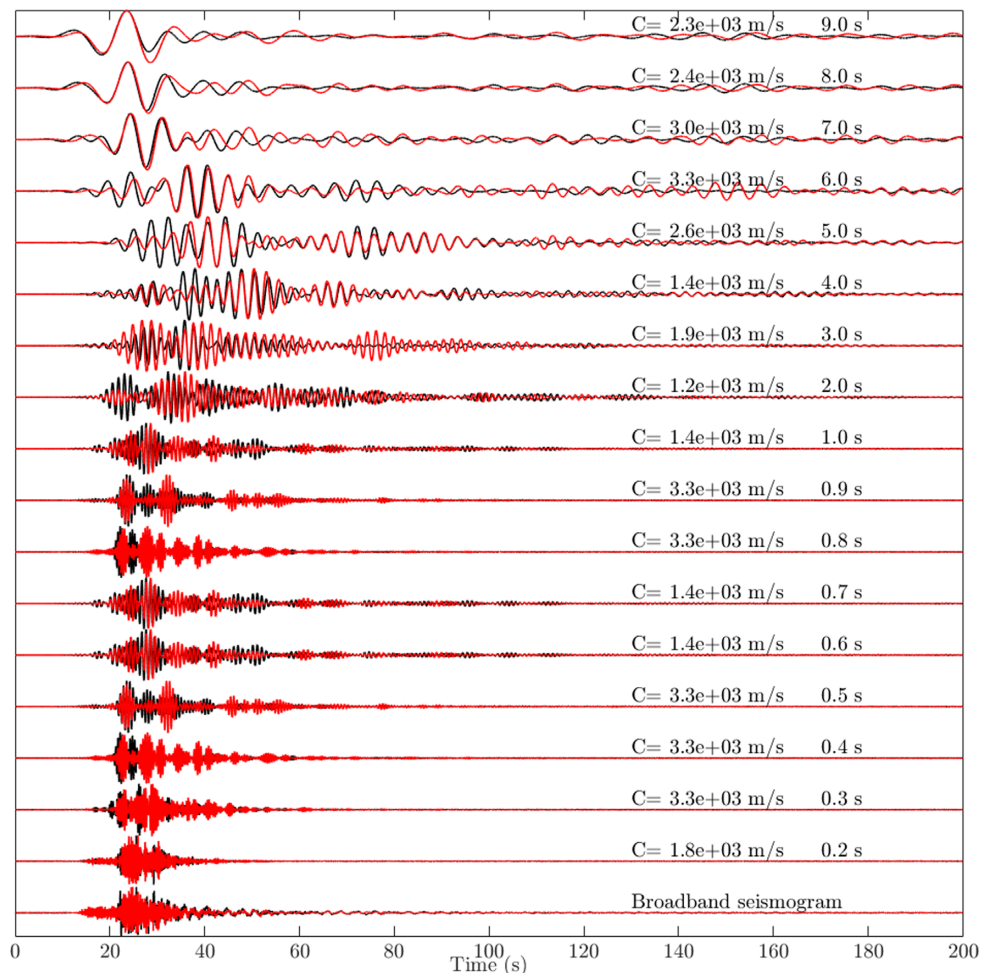
Figure 13. The Visso M_w 5.9 earthquake. Superposition of vertical rotation rate (red) and transverse acceleration (black) and determination of phase velocities as a function of central frequency of the half-octave bandpass filter. The phase-velocity values are measured by taking the ratio of the peak envelopes of the bandpass-filtered seismograms. For graphical reasons, translational and rotational traces are individually normalized to their respective maximum.

observed throughout the coda of the *P*-wave arrival, an observation which is interpreted in terms of near-receiver *P–SH* converted energy due to 3-D effects associated with the complex topography and anisotropy. Those particular coda waves, however, do exhibit a large variability in the rotation/acceleration ratio, as a likely consequence of differences in the wave path and/or source mechanism. The future steps of this experiment are to increase the span of observations in terms of both azimuthal coverage and distance. This will allow us to increase the robustness of phase-velocity measurements and to clarify the nature of the observed BAZ misfits.

REFERENCES

Aki, K. & Richards, P.G., 2009. *Quantitative Seismology,* 2nd edn, University Science Books.

Belfi, J. *et al.*, 2017. Deep underground rotation measurements: GINGERino ring laser gyroscope in Gran Sasso, *Rev. Sci. Instrum.,* **88**(3), 034502, doi:10.1063/1.4977051.

Bindi, D., Pacor, F., Luzi, L., Puglia, R., Massa, M., Ameri, G. & Paolucci, R., 2011. Ground motion prediction equations derived from the Italian strong motion database, *Bull. Earthq. Eng.,* **9**(6), 1899–1920.

Bird, P. & Carafa, M.M.C., 2016. Improving deformation models by discounting transient signals in geodetic data: 1. Concept and synthetic examples, *J. geophys. Res.,* **121**(7), 5538–5556.

Butler, R.W., Tavarnelli, E. & Grasso, M., 2006. Structural inheritance in mountain belts: an Alpine–Apennine perspective, *J. Struct. Geol.,* **28**(11), 1893–1908.

Chiaraluce, L. *et al.*, 2017. The 2016 Central Italy seismic sequence: a first look at the mainshocks, aftershocks, and source models, *Seismol. Res. Lett.,* **88**(3), 757–771.

Cochard, A. *et al.*, 2006. Rotational motions in seismology: theory, observation, simulation, in *Earthquake Source Asymmetry, Structural Media and Rotation Effects,* pp. 391–411, eds Teisseyre, R., Majewski, E. & Takeo, M., Springer.

Di Domenica, A., Bonini, L., Calamita, F., Toscani, G., Galuppo, C. & Seno, S., 2014. Analogue modeling of positive inversion tectonics along differently oriented pre-thrusting normal faults: an application to the Central-Northern Apennines of Italy, *Bull. geol. Soc. Am.,* **126**(7-8), 943–955.

Douglas, J., 2003. Earthquake ground motion estimation using strong-motion records: a review of equations for the estimation of peak ground acceleration and response spectral ordinates, *Earth-Sci. Rev.,* **61**, 43–104.

Grinsted, A., Moore, J.C. & Jevrejeva, S., 2004. Application of the cross wavelet transform and wavelet coherence to geophysical time series, *Nonlinear Process. Geophys.,* **11**(5/6), 561–566.

Igel, H., Cochard, A., Wassermann, J., Flaws, A., Schreiber, U., Velikoseltsev, A. & Pham Dinh, N., 2007. Broad-band observations of earthquake-induced rotational ground motions, *Geophys. J. Int.,* **168**(1), 182–196.

Igel, H., Schreiber, U., Flaws, A., Schuberth, B., Velikoseltsev, A. & Cochard, A., 2005. Rotational motions induced by the M8.1 Tokachi-oki earthquake, September 25, 2003, *Geophys. Res. Lett.,* **32,** L08309, doi:10.1029/2004GL022336.

Lee, W. H.K., Evans, J.R., Huang, B.-S., Hutt, C.R., Lin, C.-J., Liu, C.-C. & Nigbor, R.L., 2012. Measuring rotational ground motions in seismological practice, in *New Manual of Seismological Observatory Practice 2 (NMSOP-2),* pp. 1–27, ed. ,Bormann, P., Deutsches GeoForschungsZentrum GFZ.

Li, H., Bernardi, F. & Michelini, A., 2010. Love wave tomography in Italy from seismic ambient noise, *Earthq. Sci.,* **23**(5), 487–495.

Malinverno, A. & Ryan, W. B.F., 1986. Extension in the Tyrrhenian sea and shortening in the Apennines as result of arc migration driven by sinking of the lithosphere, *Tectonics,* **5**(2), 227–245.

McLeod, D., Stedman, G., Webb, T. & Schreiber, U., 1998. Comparison of standard and ring laser rotational seismograms, *Bull. seism. Soc. Am.,* **88**(6), 1495–1503.

Michele, M. *et al.*, 2016. The Amatrice 2016 seismic sequence: a preliminary look at the mainshock and aftershocks distribution, *Ann. Geophys.,* **59,** doi:10.4401/ag-7227.

Pancha, A., Webb, T., Stedman, G., McLeod, D. & Schreiber, K., 2000. Ring laser detection of rotations from teleseismic waves, *Geophys. Res. Lett.,* **27**(21), 3553–3556.

Peterson, J., 1993, Observations and modeling of seismic background noise, USGS open file Open-File Rep, 93-322, USGS.

Schreiber, K.U. & Wells, J.-P.R., 2013. Invited review article: large ring lasers for rotation sensing, *Rev. Sci. Instrum.,* **84**(4), 041101, doi:10.1063/1.4798216.

Schreiber, U., Igel, H., Cochard, A., Velikoseltsev, A., Flaws, A., Schuberth, B., Drewitz, W. & Müller, F., 2006. The GEOsensor project: rotations, a new observable for seismology, in *Observation of the Earth System from Space,* pp. 427–443, eds Flury, J., Rummel, R., Reigber, C., Rothacher, M., Boedecker, G. & Schreiber, U., Springer.

Scisciani, V. & Calamita, F., 2009. Active intraplate deformation within Adria: examples from the Adriatic region, *Tectonophysics,* **476**(1), 57–72.

Scognamiglio, L., 2009. Real-Time determination of the Seismic Moment Tensor for the Italian Region, *Bulletin of the Seismological Society of America,* **99**(4), 2223–2243.

Simonelli, A., Belfi, J., Beverini, N., Carelli, G., Virgilio, A.D., Maccioni, E., Luca, G.D. & Saccorotti, G., 2016. First deep underground observation of rotational signals from an earthquake at teleseismic distance using a large ring laser gyroscope, *Ann. Geophys.,* **59,** doi:10.4401/ag-6970.

Spudich, P. & Fletcher, J.B., 2008. Observation and prediction of dynamic ground strains, tilts, and torsions caused by the M_w 6.0 2004 Parkfield, California, earthquake and aftershocks, derived from UPSAR array observations, *Bull. seism. Soc. Am.,* **98**(4), 1898–1914.

Stedman, G., Li, Z. & Bilger, H., 1995a. Sideband analysis and seismic detection in a large ring laser, *App. Opt.,* **34**(24), 5375–5385.

Stedman, G.E., Li, Z., Rowe, C.H., McGregor, A.D. & Bilger, H.R., 1995b. Harmonic analysis in a large ring laser with backscatter-induced pulling, *Phys. Rev. A,* **51,** 4944–4958.

Tavarnelli, E., 1996. The effects of pre-existing normal faults on thrust ramp development: an example from the northern Apennines, Italy, *Geologische Rundsch.,* **85**(2), 363–371.

Thomson, D.J., 1982. Spectrum estimation and harmonic analysis, *Proc. IEEE,* **70**(9), 1055–1096.